

Anisotropic super-paramagnetism in cobalt implanted rutile-TiO₂ single crystals

Shalik Ram Joshi¹, B. Padmanabhan², Anupama Chanda³,

N. Shukla⁴, Vivek Malik², D. Kanjilal⁵ and Shikha Varma^{1*}

¹*Institute of Physics, Sachivalaya Marg, Bhubaneswar-751005*

²*Department of Physics, Indian Institute of Technology, Roorkee 247667, India*

³*Department of Physics, Dr. Hari Singh Gour University, M.P 470003, India*

⁴*Department of Physics, NIT Patna, 800005, India*

⁵*Inter University Accelerator Center, New Delhi 110067, India*

(Dated: October 6, 2018)

We study the magnetic properties of single crystals of rutile-TiO₂ implanted with cobalt for various fluences ranging from 1×10^{16} to 1×10^{17} . For lower fluences, the nature of magnetism is not affected by the Co substituting Ti sites forming $\text{Ti}_{1-x}\text{Co}_x\text{O}_2$. From a fluence of 5×10^{16} onwards, the magnetic behaviour changes drastically due to formation of hcp cobalt clusters which are detected by x-ray diffraction. For the highest fluence sample (1×10^{17}) we also detect formation of CoTiO_3 phase. The Co nano-clusters give rise to super-paramagnetism which is highly anisotropic w.r.t the crystallographic directions of TiO₂. The temperature and field dependent magnetization was studied in detail for magnetic field (H) along $\langle 001 \rangle$ and $\langle 1\bar{1}0 \rangle$ directions. The temperature variation of zero field cooled (ZFC) and field cooled (FC) magnetization shows a much higher blocking temperature (T_B) along $\langle 1\bar{1}0 \rangle$. Similarly the scaling of magnetization isotherms above T_B is seen only when the field is parallel to $\langle 1\bar{1}0 \rangle$ direction. With field along this direction, the magnetization shows near saturation at a much smaller field compared to that of $\langle 001 \rangle$ direction. With increase in fluence we find increase in particle size (from 2.5 to 4.5 nm diameter) and size distribution by fitting our magnetization isotherms to Langevin function assuming a lognormal distribution of particle sizes. Below T_B , at the lowest temperatures we observe that the $M-H$ curves show a wide hysteresis loop when the field is along $\langle 1\bar{1}0 \rangle$ direction suggesting the highly oriented nature of the clusters. The Co nanoclusters possess an “easy” and “hard” axis of magnetization coupled by the magnetocrystalline anisotropy of $\text{Ti}_{1-x}\text{Co}_x\text{O}_2$. In addition, at $T=2$ K we observe a crossover in the magnetization vs field isotherms between the two field directions in the samples with Co fluences of 8×10^{16} and 1×10^{17} which is not seen above T_B . The origin of this crossover, is discussed briefly in terms of anisotropic paramagnetism arising from cobalt present in $2+$ ionic state with $S = 3/2$.

I. INTRODUCTION

The study of magnetism in nano-particles has gained enormous interest in last two decades from technological as well as fundamental perspectives¹. In nanoscale systems, magnetic nature can be drastically different, compared to a bulk, since surface effects play crucial role in determining this behavior such that properties as diverse as ferromagnetism, anti-ferromagnetism, super-paramagnetism (SPM) or spin-glass(SG) like behavior are observed¹⁻⁴. Among these, SPM is a property that crucially depends on the size of the nano-particle and shows magnetic moment that is proportional to the particle- volume³. SPM nano-sized cluster can exhibit giant magnetic moment (sometimes as high as few thousand μ_B) which is randomly oriented in the absence of external field. The particles are non-interacting, except for a weak dipole interaction. Thus, an ideal super-paramagnet should exhibit *paramagnetic behavior*, i.e follow Curie - Weiss law, but with a large effective moment and a non-hysteretic $M - H$ curve up to 0 K. However, effects of magneto-crystallinity as well as surface and shape anisotropy alter this behavior such that a real super-paramagnet shows deviations from the Curie-Weiss law at the non-zero temperatures⁵. The super-paramagnetic clusters possess a uniaxial anisotropic direction which is random in direction for each SPM particle. Thus every individual nano-particle has its corresponding easy axes of magnetization.

As the system is cooled through the SPM state, there comes a characteristic temperature called the blocking temperature (T_B). Above T_B , the magnetic moment of the individual SPM particle is oriented randomly like a normal paramagnet, which can rotate freely under the influence of external field. Below T_B , the individual SPM particle has its magnetic moment blocked along its respective easy anisotropy axis. This temperature is prominently seen as a bifurcation of zero field cooled (ZFC) and field cooled (FC) magnetization. Associated with this temperature is an energy barrier U , which is the energy required for the individual magnetic moment to flip its direction along the two easy axes directions. The time for flip is giving by the characteristic equation³,

$$\tau = \tau_0 \exp\left(\frac{U}{k_B T}\right) \quad (1)$$

Here τ_0 is the limiting relaxation time, k_B is the Boltzmann constant, T is the temperature and U is the potential barrier. The blocking temperature is affected by individual particle volume and their distribution⁶.

SPM behavior has been shown by several transition metals and their alloys when incorporated in non-magnetic host matrices, such as by Co multilayers on Al_2O_3 ⁶, nano-crystallites of CoFe_2O_4 ⁷, nano-powdered CoPt_3 alloys⁸ and Ni nano-particles on SiO_2 ⁵. These compounds show a near perfect SPM behavior with a low blocking temperature and a universal scaling behavior⁵ in $M - H$ curves.

Incorporating Co in TiO_2 , however, has been demonstrated to form a dilute magnetic semiconductor (DMS) system that shows room temperature ferromagnetism⁹. DMS materials, achieved by introducing small concentration of transition metal or non-magnetic material in a semiconductor, exhibit ferromagnetic/ anti-ferromagnetic properties that are useful in spintronic devices. DMS is demonstrated by many systems like Co/Mn substituted in TiO_2 , ZnO or Mn doped in narrow band gap semiconductors like GaAs, InAs¹⁰⁻¹³ etc. For Co doped TiO_2 , magnetic properties have been investigated, in rutile and anatase forms of bulk as well as thin TiO_2 ^{9,14-16} films that were prepared by various methods like pulsed laser deposition, molecular beam epitaxy, magnetron sputtering, metal organic chemical-vapor deposition and sol-gel technique^{17,18}. In spite of extensive studies, origin of observed ferromagnetism in this system is still unclear. Investigations suggest that cobalt ions in thin TiO_2 films exist in a +2 oxidation state forming

$\text{Ti}_{1-x}\text{Co}_x\text{O}_2$, which is ferromagnetic in nature¹⁹. Most of the preparation techniques produce precipitation of cobalt metallic nano-clusters which could also be responsible for this observed ferromagnetism¹⁹. First principles calculations for Co substituting Ti sites in rutile as well as anatase TiO_2 show creation of Co $3d$ bands at the Fermi energy implying metallicity^{20,21}. Also a net magnetic moment of $\sim 0.6\mu_B$ occurs at the Co site suggesting that Co is in low spin state.

Implantation is a less explored method for introducing magnetism in a non-magnetic system. By this technique, small concentrations of dopants can be introduced, at well defined depth, in the host. Systems produced in this fashion can show many interesting electronic and magnetic properties²². Mn implanted GaP displays enhanced magnetism with a transition temperature above 300 K²³. Mixed phases of ferromagnetism and super-paramagnetism have been observed after high fluence (1.5×10^{17} ions/cm²) implantation of Cobalt in rutile $\text{TiO}_2(001)$ single crystals^{24,25} which forms the basis of present study. Few studies have also shown SPM behavior in Co thin films on TiO_2 ²⁶. However, none of these studies have investigated the anisotropic nature of magnetization along different crystallographic directions, or the role of inter-cluster interactions.

The present study investigates the magnetic behavior after Cobalt implantation in rutile $\text{TiO}_2(110)$ single crystals. Surprisingly, a super-paramagnetic behavior is observed here instead of the expected ferromagnetic behavior from TiO_2 which is a DMS material. Here a detailed study of magnetic behavior, originating especially from super-paramagnetism, both above and below the blocking temperature, is presented. Interestingly, the super-paramagnetic behavior here is anisotropic in nature, i.e. non-equivalent along the two crystallographic axes of TiO_2 . Development of $\text{Ti}_{1-x}\text{Co}_x\text{O}_2$ phase and Cobalt nano-clusters give rise to properties not observed before in SPM or DMS based systems.

II. EXPERIMENTAL DETAILS

Commercially available single crystals ($5\text{mm} \times 5\text{mm} \times 1\text{mm}$) of TiO_2 (from Matek) with $\langle 110 \rangle$ crystallographic direction perpendicular to the surface, were implanted with cobalt ions at room temperature with fluences of 5×10^{16} , 8×10^{16} and 1×10^{17} ions/cm². These samples have been labeled here as A, B and C, respectively. In addition, implantation was also carried out at two lower fluences of 1×10^{16} and 3×10^{16} ions/cm². Co ions were implanted in TiO_2 with an energy of 200 keV. The penetration depth of Co in TiO_2 has been evaluated using SRIM to be $\sim 90\text{nm}$ ²⁷. The structural modifications have been investigated using X-Ray Diffraction (XRD), both in conventional $\theta - 2\theta$ geometry as well as in grazing angle geometry, on a Bruker diffractometer, using Cu K_α source. For grazing incidence XRD studies, an incidence angle of 2° was chosen. Magnetic measurements were performed using a commercial Superconducting Quantum Interference Device (SQUID). Temperature dependence of magnetization (M) has been obtained for Zero-Field Cooled (ZFC) as well as Field Cooled (FC) conditions in a field of 0.05 T. Magnetization (M) vs. magnetic field (H) measurements have been carried out at various temperatures ranging between 2 and 300 K. The magnetic measurements have been carried out with H parallel (H_{\parallel}) as well as perpendicular (H_{\perp}) to $\langle 001 \rangle$ crystallographic direction of the TiO_2 crystals.

III. RESULTS AND DISCUSSION

A. X-Ray Diffraction

Fig. 1 displays the XRD results from pristine TiO_2 as well as after it is implanted with Co at the fluences of 5×10^{16} , 8×10^{16} and 1×10^{17} ions/cm² (samples A, B and C). Fig. 1(a) shows a sharp feature at 27° both prior to and after implantation. Fig. 1(a) shows the $\langle 110 \rangle$ Bragg reflection at 27° in the pristine and implanted TiO_2 crystals. The Bragg peaks show slight shift and become little broader upon Cobalt implantation indicating generation of some stress as well as substitutional incorporation of Co in TiO_2 lattice with the formation of $\text{Ti}_{1-x}\text{Co}_x\text{O}_2$ ($x < 0.01$) at low fluences²⁸. Fig. 1(b) presents the normal XRD ($39\text{-}50^\circ$) results which show presence of Cobalt clusters at the highest fluence of 1×10^{17} ions/cm², not observed for lower fluences. Here, the broad feature at $\sim 47.4^\circ$ reflects the formation of hexagonal closed packed (hcp) Cobalt (1011) clusters. In addition, the feature at $\sim 40.7^\circ$ suggests formation of a secondary CoTiO_3 (210) phase²⁹. Development of Cobalt clusters is also reflected by the grazing incidence XRD studies (fig. 1(c)) where hcp $\text{Co}(11\bar{1}0)$ is observed at 76° for the samples B and C but not for the sample A. Based on the width of hcp-Co Bragg peak, particle size of hcp-Co cluster has been determined to be ~ 7 nm. The effect of cluster formation on the magnetic properties is discussed below.

B. Magnetization vs. Temperature

The temperature variation of magnetization for both pristine as well as implanted samples were measured with magnetic field (H) pointed along two crystallographic directions of TiO_2 viz. $\langle 001 \rangle$ (H_{\parallel}) and $\langle 1\bar{1}0 \rangle$ (H_{\perp}). Fig. 2(a) (inset) displays the ZFC-FC plots for the pristine sample. Though the trends in magnetization are the same, along both the field directions, magnetic moment (M) is higher along H_{\parallel} . This suggests H_{\parallel} ($\langle 001 \rangle$) to be the easy (anisotropic)-axis in pristine TiO_2 . Below 20 K, a downward trend in the ZFC plot is observed which rises again upon further decrease in temperature. Ideally, the pristine sample should be non-magnetic due to the empty d orbital of Ti^{4+} . However, Van Vleck paramagnetism and a weak defect induced magnetic ordering is observed due to the presence of O and Ti type vacancies and other defects^{30,31}.

For small Co implantation fluences (1×10^{16} and 3×10^{16} ions/cm²), though there is a slight increase in the magnetization (data not shown), the nature of ZFC-FC curves remain similar to the pristine. At these low fluences, lattice remains paramagnetic with Co ions substitutionally incorporated in the TiO_2 lattice and net magnetic behavior unaltered compared to pristine. However, the magnetic moment is higher for H_{\perp} indicating this to be the preferred magnetization direction with Co substitution.

For the Co fluence of 5×10^{16} ions/cm² (sample A), a drastically different magnetic nature compared to the pristine is observed. Fig. 2(a) shows the ZFC-FC plots for both the field directions. For H_{\parallel} , a bifurcation in ZFC is noticed at 8 K, while for H_{\perp} this is at 30 K. With increasing fluence, i.e. for sample B and C, the bifurcations shift to much higher temperatures. Fig. 2(b) shows the ZFC-FC plots for samples B and C in both field configurations. The nature of splittings in these plots indicate that samples A, B and C show super-paramagnetism, with arrows indicating the respective blocking temperatures (T_B). The large increase in T_B with fluence indicates an increase in the particle size while the broadening of the transition around T_B indicates a large variance in particle diameters. For all the

three samples, M and T_B are considerably higher for field along H_\perp compared to H_\parallel (also see table 1). At the highest fluence 1×10^{17} ions/cm² (sample C), the difference in T_B of 80 K between H_\parallel and H_\perp , indicates that this system is very anisotropic.

For H_\parallel field, magnetization in samples B and C appears nearly constant, with temperature, above T_B . The decrease in magnetization is much slower than the expected Curie-Weiss like decrease in SPM systems. However for H_\perp field, a decrease in magnetization with temperature is observed similar to that expected in SPM systems. Fig. 2(b) (inset) shows a plot of inverse susceptibility (χ^{-1}) as a function of temperature, for sample C, along both the field directions. Similar to a paramagnetic system, χ^{-1} should show a linear increase with temperature. However, here this is only observed in the case of H_\perp direction. The intercept on the T-axis is negative, indicating presence of some antiferromagnetic couplings in the system, similar to the pristine. For H_\parallel , χ^{-1} is almost constant above T_B (fig. 2(b) inset).

Thus the magnetic moments of the clusters in this cobalt implanted system are rotatable, due to external field and temperature, only when the field is along H_\perp direction. In a typical SPM, well below T_B , the ZFC susceptibility increases with increasing temperature, suggesting that more nano-particles get unblocked and contribute to the susceptibility. Most of the particles get unblocked near T_B and the system becomes an SPM for $T > T_B$. Thus irrespective of field direction all SPM particles get unblocked above T_B and display a Curie-Weiss like behavior with increasing temperature. Such a behavior is observed, above T_B , in our system only for H_\perp . For field along H_\parallel , the magnetization above T_B remains nearly constant with increasing temperature. This suggests that along this direction, only the smaller nano-particles get unblocked above T_B , whereas the larger particles remain blocked. Combined anisotropy due to the Co clusters and $\text{Ti}_{1-x}\text{Co}_x\text{O}_2$ will be responsible for this observation, as will be discussed below.

C. Magnetization vs. Field

1. Above Blocking temperature

Fig. 3 shows the magnetization isotherms, above T_B , for pristine and cobalt implanted samples. M - H plots for the pristine TiO_2 , at 2 and 300 K, are shown in the inset (of fig. 3(a)) for H_\parallel and H_\perp . At 300 K, the magnetization rises linearly as expected for a paramagnetic TiO_2 , without attaining any saturation. A small (< 20 Oe) coercivity has also been observed. Moreover, the magnetization is higher along H_\parallel (than H_\perp) indicating this to be the easy axis of magnetization in the pristine sample. Similar behavior is also observed at 2 K. The magnetization curve for Sample A at 100 K along H_\perp is shown in fig. 3(a) and shows a saturation-like behavior near 1 T. This curve also displays a very small coercivity of 30 Oe. At this fluence the cobalt concentration in TiO_2 lattice is small and consequently the Co induced magnetic moment is comparable to the pristine. Assuming that the magnetization from the host lattice and from implanted ions are independent in any implanted system, so the contribution to magnetization of the former has been subtracted from that of all the implanted samples. After subtracting the pristine magnetization, the magnetization plots show a saturation like behaviour for all temperatures, which is the true behaviour of the SPM system.

The magnetization plots for samples B and C, at 300 K, are shown in fig. 3 for H_\parallel and H_\perp . Both the samples show

higher magnetization when the field is along H_{\perp} (than H_{\parallel}). While the easy-axis in pristine is along H_{\parallel} , these (B and C) show higher magnetization for H_{\perp} which indicates a reversal in the preferred direction of anisotropy. Moreover for both the samples B and C, the slope of magnetization at low H, is much steeper for fields along H_{\perp} than H_{\parallel} . As a result, the near-saturation like behavior is attained faster (at field ~ 0.2 T) in the former case than in the latter case where saturation is achieved at fields around 1 T. Ideally for an SPM system, the M - H isotherms should be reversible³. However both samples B and C, show a mild irreversible behavior. For H_{\perp} , small coercivities of nearly 60 and 90 Oe are observed for samples B and C. Coercivities are smaller along H_{\parallel} .

For an SPM system, a plot of M/M_S vs. H/T (M_S is saturation magnetization) should scale into a single universal curve⁶. Here, no scaling has been observed for sample A. Samples B and C also do not show any scaling for field along H_{\parallel} . However for H_{\perp} field, interestingly, scaling behavior is displayed (see fig. 3(d)). The scaled curves for sample B show that though the scaling exists, there are some deviations. A possible reason can be the existence of long ranged antiferromagnetic couplings due to the formation of $\text{Ti}_{1-x}\text{Co}_x\text{O}_2$, that results in an effective molecular field which hinders complete SPM-like behavior at this stage. For samples C, a nearly perfect scaling is observed indicating a good SPM character. Absence of scaling along H_{\parallel} can be due to the anisotropic effects that restrict free rotation of magnetic moments, of the nano-particles, for field applied along this direction. Thus similar to ZFC-FC plots of fig. 2, the magnetization results of fig. 3 show that the SPM-like behavior is observed in samples B and C only, when the field is applied along H_{\perp} .

In a superparamagnet, there exists a distribution of magnetic moments due to the variations in the particle size of the nanoclusters. Hence, the net magnetization is given as a weighed sum of the Langevin function³²,

$$M(H, T) = \int_0^{\infty} \mu L\left(\frac{\mu H}{k_B T}\right) f(\mu) d\mu \quad (2)$$

where $L(x) = \coth(x) - 1/x$ is the Langevin function, $f(\mu)$ is the distribution of magnetic moments, given by a log-normal distribution⁵,

$$f(\mu) = \frac{1}{\sqrt{2\pi}\mu\sigma} \exp\left[-\frac{\ln^2\left(\frac{\mu}{\mu_0}\right)}{2\sigma^2}\right] \quad (3)$$

Here μ_0 is the median of distribution and σ is the width of this distribution. The mean magnetic moment $\mu_M = \mu_0 \exp(-\sigma^2/2)$. Assuming all the nano-particles to be spherical, $\mu_0 = \pi M_S D^3/6$. Here, D is the diameter of particles and $M_S (= 1.56 u_B)$ is the saturation magnetization of bulk cobalt. The above expression holds true for $T \gg T_B$, where the role of anisotropy can be neglected.

In many SPM systems, equation (2) has been shown to yield good results for magnetization well above T_B . The fittings for the magnetization curves, using this eqn. (2), have also been shown in fig. 3(b,c) for samples B and C when the fields is along H_{\perp} . Fittings of the magnetization curves have been utilized to obtain average magnetic moment (μ_M), particle size (D) and standard deviation (σ) and are listed in table 1. With increasing fluence there is a systematic increase in the average magnetic moment as well as the particle diameter. In addition, the deviation σ also considerably increases from sample A to C. This is also observed in the ZFC-FC plots, wherein sample A displays a sharper transition while sample C shows a broader transition.

2. Below blocking temperature

The magnetization curves for the implanted samples below T_B , at 2 K, are presented in fig. 4. Inset shows the magnetization curves of sample A for both H_\perp and H_\parallel . Small coercivity is observed along both these fields. Magnetization curves for the pristine at 2 K are similar to those of sample A. Also as demonstrated by sample A (fig. 4 inset), the magnetization in pristine does not saturate even at high fields (2 T) but rather continues to increase, indicating a paramagnet- like behavior.

Fig. 4 shows the hysteresis behavior of samples B and C along H_\parallel and H_\perp . For samples B and C, coercivities (H_C) as large as 1500 and 1800 Oe, respectively, are observed for H_\perp field. These coercive fields are nearly 3 times larger than those observed for Fe implanted TiO_2 ³³ or for nano-Cobalt systems prepared by other methods³⁴.

For both the samples B and C, the magnetization ($M - H$) plots display a near saturation-like behavior above 1 T (fig. 4). Moreover, the slope (dM/dH) here at 2 K is higher than that observed above T_B at 300 K (fig. 3(b,c)). A crossover in M between the two field directions (indicated by the arrows in fig. 4) is also observed at 2 K for both the samples. This suggests an additional contribution to the magnetization at low temperatures and high fields which will be discussed below in the section on *anisotropic paramagnetism*. For 1.5 T field, both the samples B and C show a near-saturation like behavior with $M_S \sim 0.8$ and $1.2 \mu_B/\text{Co atom}$, respectively. These values are considerably lower than the saturation magnetization ($1.56 \mu_B/\text{Co atom}$) for bulk cobalt²⁴. Since the presence of isolated Co-atoms or sub-nano few-atom Co clusters will effectively not contribute to the magnetization, this observation suggests presence of some Co atoms or smaller clusters in the TiO_2 lattice. Only the nano-dimensional or bigger Co clusters give rise to the observed magnetization and estimates here show that for samples A, B and C nearly 22, 43 and 67% of the implanted cobalt atoms, respectively, form such clusters.

Starting from 2 K, the width of hysteresis loop decreases on increasing the temperature, in both the field directions for samples B and C. $M - H$ loop for both the samples display trends like a hard ferromagnet, similar to metallic Fe and Co. The hysteresis loop appears like a “parallelogram” for H_\perp , indicative of the easy axis of magnetization, but narrow “ribbon-like” for H_\parallel , similar to the hard axis of a ferromagnet.

IV. DISCUSSION

A. Anisotropy

1. Super-paramagnetic region

We briefly discuss the effect of anisotropy on the magnetic behaviour of Co nano clusters in the super-paramagnetic regime. We demonstrate that the Co nano-particles are not randomly oriented, like usual SPM clusters, rather have a fixed easy axis direction even above the blocking temperature. When $T \gg T_B$, effects of uniaxial anisotropy can be neglected and magnetization can be completely described by eqn. (2). However as temperature reduces, effects of anisotropy become non-negligible and the magnetization cannot be described in a simple analytical manner as in eqn. (2). For a system of SPM clusters, each with a random anisotropy direction, anisotropy K , saturation magnetization M_S and fixed volume V , the magnetization is obtained from the Hamiltonian, $\mathcal{H} = -V(M_S H \cos(\alpha) + K \cos^2(\theta))$. Here, the first term corresponds to the external magnetic field energy and the second term corresponds

to easy axis anisotropy energy. The external magnetic field H makes an angle α with the magnetization and λ with the easy axis, while θ corresponds to the angle between the easy axis and the magnetization. The full configuration is described in detail by Morup *et al.*³⁵, in which the net magnetization $M(H, T, K)$ is obtained after integration over the angles θ , α , the azimuthal angle ϕ and finally over all possible directions of applied field. However, in our case we consider two extreme cases viz. $\lambda = 0$ and $\pi/2$, corresponding to the easy axis (H_{\perp}) and the hard axis (H_{\parallel}) respectively.

Using this formalism, the magnetization curves for the two λ values have been calculated for $T = 100$ K, $M_S = 1.2 \mu_B$, $K = 5 \times 10^5 \text{ J/m}^3$, $V = 41 \times 10^{-27} \text{ m}^3$ which corresponds to the sample with highest fluence, and are shown in fig. 5. The nature of theoretical curves, for two field directions, agree well the experimental isothermal magnetization results shown in fig. 4. Thus the theoretical results clearly show that applying the fields along $\langle 1\bar{1}0 \rangle$ and $\langle 001 \rangle$ crystallographic directions is exactly equivalent to applying magnetic fields along the “easy” and “hard” axis of the Co clusters.

This confirms that the magnetic anisotropy directions of the clusters, in the present system, are not entirely random as expected in a super-paramagnetic system but are effectively along the $\langle 1\bar{1}0 \rangle$ crystallographic direction. This also suggests that the anisotropy of the Co clusters is coupled to the magneto-crystalline anisotropy of the $\text{TiO}_2/\text{Ti}_{1-x}\text{Co}_x\text{O}_2$ lattice which would be subsequently discussed.

2. Anisotropy Below the Blocking Temperature

The $M - H$ plots of samples B and C for 2 K show a large anisotropic character similar to that of the bulk metallic Co. The uniaxial anisotropy of the system is given by $K_{\mu} = M_S H_K / 2$, where H_K is the anisotropy field³³, which is also the saturation field for the hard axis. In both the samples, the saturation along the hard axis (H_{\parallel}) is attained at $H_K \sim 1.2$ T, suggesting anisotropy constant of 2.5×10^5 Joule/m³ and 5.39×10^5 Joule/m³ for samples B and C, respectively. These values are smaller than the anisotropy constant of 7.5×10^5 Joule/m³ observed for the bulk cobalt at 5 K⁸. This is due to the presence of some isolated (substituted) atoms and sub-nano clusters in the TiO_2 lattice which also led to (see fig. 4) lower saturation magnetization for samples B and C, compared to the bulk Cobalt. Bulk cobalt has a uniaxial anisotropy along the hexagonal c direction which corresponds to the easy axis¹⁴. Thus in samples B and C, it can be expected that the c axis of the individual cobalt clusters should be aligned along the $(1\bar{1}0)$ direction of TiO_2 crystal. Similar oriented metallic clusters have also been observed in Fe implanted TiO_2 where $\langle 1\bar{1}0 \rangle$ direction (H_{\perp}) of TiO_2 is the easy axis³³. However, does not show any specific crystallographic orientation of the Co clusters. This could be because, unlike cubic symmetry of Fe, the hexagonal symmetry of Co is not compatible with the tetragonal TiO_2 crystal (see fig. 1). Hence, the origin of the strong anisotropic character of the SPM clusters could be due to the combined effect of the uniaxial anisotropy of the hexagonal Co clusters along with the magneto-crystalline anisotropy of the host $\text{TiO}_2/\text{Ti}_{1-x}\text{Co}_x\text{O}_2$ lattice.

In switching of the easy axis, from being along H_{\parallel} ($\langle 001 \rangle$) prior to implantation to H_{\perp} ($\langle 1\bar{1}0 \rangle$) after implantation, it is assumed that the anisotropy of Co spins occupying Ti sites play a significant role. To verify this, first principle calculations have been carried out to determine the magneto-crystalline anisotropy energy of $\text{Ti}_{1-x}\text{Co}_x\text{O}_2$ using VASP³⁶. The calculations were performed for three spin directions of Co spin: along H_{\parallel} , along H_{\perp} and along $\langle 110 \rangle$. The net magnetic moment $\sim 0.7 \mu_B$ obtained here is lower than $1 \mu_B$ expected for the $S=1/2$ system, suggesting an

itinerant character. Among the three spin configurations, the system has the lowest energy when spin is along H_{\perp} , while energy is highest along H_{\parallel} direction. This is in agreement with the experimental results observed here. The difference in energy, in these two directions, is approximately -0.5 meV/Co i.e. nearly ~ 5 K. These results indicate that the magnetocrystalline anisotropy of Co in $\text{Ti}_{1-x}\text{Co}_x\text{O}_2$ determines the easy and hard axis and leads to highly anisotropic super-paramagnetism in TiO_2 .

3. Anisotropic paramagnetism

In addition to the anisotropic effects of super-paramagnetic Co clusters, an additional anisotropy from paramagnetic Co ions has also been observed here. In the magnetization isotherms of samples B and C above T_B (fig. 3), magnetization is observed to be nearly constant for fields higher than 1 T, especially for field along H_{\perp} . However in the blocked region, at 2 K, an increase in dM/dH for samples B and C is observed (see fig. 4). This is in contrast to the usual SPM systems where M remains almost constant with increasing H. A possible reason for this could be the presence of uncompensated paramagnetic Co spins. In addition, a cross over in magnetization between the two field directions (shown by arrow in fig. 4) is also observed. The cobalt that occupies Ti sites in TiO_2 lattice should be in a 4^+ state corresponding to the $S=1/2$ system, as also observed in the first principles calculations carried out here. In $S=1/2$ system, the single ion anisotropy does not affect the magnetic behavior. The unusual cross-over behavior can be explained qualitatively by considering the presence of Co^{2+} ions, i.e. $S=3/2$ system. The crossover observed here then arises due to presence of the single ion anisotropy of this $3/2$ spin state. Origin of Co^{2+} is via formation of CoTiO_3 nanoclusters whose presence in sample C has been observed by XRD (fig. 1). In addition, Co^{2+} also exists as Ti_2O_3 . XPS studies have shown that along with a Ti^{4+} state, a small percentage of Ti^{3+} also develops for samples B and C and increases with the fluence²⁸. Still, the main source of Co^{2+} spins here is CoTiO_3 and though it has been observed only for sample C, it is likely that smaller amounts will be present in sample B also.

Similar paramagnetic anisotropy has been observed in the magnetization of Co:ZnO thin films³⁷. Ney et al.^{37,38} have discussed the magnetization in terms of an *effective spin Hamiltonian* with an anisotropy along the crystallographic c axis (referred as z axis) of $\text{Zn}_{1-x}\text{Co}_x\text{O}$ films. Here, effective spin Hamiltonian has been applied to understand the anisotropic paramagnetic behavior observed in fig. 4. Remarkably, no crossover was observed when anisotropy was along \hat{z} axis (i.e. along H_{\parallel} : $\langle 001 \rangle$), rather it was observed when \hat{x} direction (along H_{\perp} : $\langle 1\bar{1}0 \rangle$) of the spin was considered to be the axis of single ion anisotropy (geometry of the present system is shown in fig. 5). Hence, a modified $S = 3/2$ spin Hamiltonian was used here and is discussed below:

$$\hat{H}_{spin} = \mu_B g_{\parallel} H_z S_z + \mu_B g_{\perp} (H_x S_x + H_y S_y) + Q S_x^2, \quad (4)$$

Here the magnetic state is characterized by two g factors, g_{\parallel} (2.238) and g_{\perp} (2.276), and the zero field splitting constant Q ³⁷. In the above equation, Q corresponds to single ion anisotropy of $S=3/2$ system, due to Co^{2+} , along the \hat{x} direction. Spin Hamiltonian has been applied to calculate the energy levels of the $S = 3/2$ system $|M_S \rangle = |-3/2 \rangle \dots | +3/2 \rangle$ by using the matrix $\langle M_S | \hat{H}_{spin} | M_S \rangle$ for $H \parallel \hat{z}$ ($H \parallel H_{\parallel}$) and $H \parallel \hat{x}$ ($H \parallel H_{\perp}$). Diagonalization of the matrix provides four eigenvalues along each direction. These energy values $E_{i,a}$ ($i : M_S$ values and $a = H \parallel \hat{z}, \hat{x}$) were used to calculate the magnetization $M = (\partial F / \partial T)_H$ of the magnetic free energy $F = -k_B T \ln(Z_{i,a})$ using the partition function $Z_{i,a} = \sum_i e^{-E_{i,a}/k_B T}$.

Fig. 6 shows the $M - H$ curves calculated at $T = 2$ K using the spin Hamiltonian for varying strengths of Q . The strength of zero-field splitting Q was varied from 0 K to 4 K and its role on the anisotropy of the $M - H$ curves was investigated. For $Q = 0$ K the $M - H$ curves calculated for $H \parallel H_{\parallel}$ and $H \parallel H_{\perp}$ show no cross-over. The shape of $M - H$ curves for $H \parallel H_{\parallel}$ do not show much change upon increasing Q . On the other hand, the $M - H$ curves for $H \parallel H_{\perp}$ show a decreasing slope with increasing Q . This becomes responsible for an increase in anisotropy, and a cross-over (marked by the arrow) is seen for $Q = 4$ K. This plot calculated at $T = 2$ K can be compared with the experimental data presented in fig. 4 and displays a similar anisotropic behavior. Moreover, interestingly the effective Hamiltonian calculations for $S = 3/2$ system of Co in TiO_2 here show that the anisotropy is observed when \hat{x} (H_{\perp}) direction of the spin is considered to be the axis of single ion anisotropy, unlike the \hat{z} (H_{\parallel}) direction in Co:ZnO system³⁷.

B. Dipole and inter-particle exchange interactions

In the blocked region of a super-paramagnet, the parameters of importance are coercivity H_C , and the reduced remanence ($m_R = M_R/M_S$). For a system of non-interacting particles with random anisotropy axes, the reduced remanence should be ~ 0.5 . The values of M_R and H_C are much smaller for field along H_{\parallel} axis (fig. 4), since it corresponds to the hard axis of the clusters. Hence in this section field along H_{\perp} direction is discussed. With increase in fluence the reduced remanence increases along with the coercive field. At 2 K, sample A shows the lowest m_R of 0.2, while samples B and C show values of 0.47 and 0.55, respectively, for field along the H_{\perp} direction. The highly reduced remanence in sample A indicates a dominating presence of antiferromagnetic interactions³⁹ in the system. Similar to the reduced remanence, the temperature dependent coercivity $H_C(T)$ for a *system of randomly oriented and non interacting particles* displays a behavior given by⁵,

$$H_C(T) = H_{CO} \left(1 - \left(\frac{T}{T_B^0} \right)^{1/2} \right). \quad (5)$$

with $H_{CO} = K_{ub}/M_{sb}$, where K_{ub} and M_{sb} are the anisotropy and saturation magnetization of bulk cobalt. T_B^0 is the Blocking temperature at zero field, $T_B^0 = \frac{K_{\mu} \langle V \rangle}{k_B \ln(\tau_m/\tau_0)}$, where K_{μ} is the uniaxial anisotropy constant, $\langle V \rangle$ is the average particle volume, τ_0 and τ_m are the characteristic limiting relaxation time and the measurement time. K_B is the Boltzman constant. Fig. 7 shows $H_C(T)$ as a function of reduced temperature $k_B T/K_{\mu} \langle V \rangle$ for samples B and C along the H_{\perp} . Here $\langle V \rangle$ corresponds to the average volume and has been evaluated using the size(D) of the clusters as mentioned in table 1. In order to directly observe the linear relation, inset of fig. 7 also displays a plot of H_C against $T^{1/2}$ for samples B and C. For sample B, a linear relation has been observed up to $T \sim 50$ K. However above this temperature, deviations occur as T approaches T_B ($=65$ K). In sample C also, H_C shows deviations beyond ~ 50 K, a temperature which is much lower than its T_B ($=150$ K). Also, the extrapolation of $H_C(T)$ to 0 yields values of $T_B \sim 64$ K and 100 K for samples B and C, respectively, which are lower than the observed blocking temperatures. The deviation from linearity suggests a strong presence of inter-particle interactions between the Co clusters

The most prominent interaction among the clusters is the inter-particle dipole interaction. In addition, there also exists presence of inter-particle exchange interactions. Using Monte-Carlo (MC) simulations, Kechrakos and Trohidou et al.^{40,41} have investigated the role of inter-particle dipole and exchange interactions in determining the coercivity and remanence of the magnetization, in the blocked region, for a system of SPM nano-particles with random uniaxial

anisotropic directions. The variations in m_R and H_C have been studied as a function of increasing volume fraction of the magnetic nano-particles. Since the size and number of the Co nano-clusters formed inside TiO_2 , increase with fluence, we expect an increase in the volume fraction of nano-particles. Thus with fluence, the inter-particle dipolar strength increases, which has a demagnetizing effect on the magnetization, causing a decrease in m_R and H_C . This suggests that in addition to the dipole interaction, there exists a strong inter-particle exchange interaction between the clusters which can even cause complete ferromagnetic alignment between the clusters. The itinerant nature of the Co occupying Ti sites, can produce this carrier mediated exchange interaction between the clusters. Presence of competing dipolar- interactions has also been observed via ZFC-FC curves.

V. CONCLUSION

Present study investigates the magnetic properties of single crystals of rutile TiO_2 after they are implanted with Co ions. ZFC- FC curves show presence of super-paramagnetic character above T_B . This SPM behavior, seen due to the development of Cobalt nano-clusters in the host lattice, is surprisingly anisotropic along the crystallographic directions of the crystal. With this anisotropy, SPM behavior is observed only along the $\langle 1\bar{1}0 \rangle$ (H_\perp) direction which behaves as an easy-axis of magnetization, and not along $\langle 001 \rangle$ (H_\parallel). Analysis with Langevin function -fitting considers a lognormal distribution of cluster sizes and yields a systematic increase in magnetic moment as well as particle volume with fluence, above T_B . For sample C, a linear behavior in inverse susceptibility, higher T_B and a good M/M_S vs. H/T scaling is observed only when field is in H_\perp direction. Such anisotropy is very unexpected and shows that though along this H_\perp direction magnetic moments are easily rotatable, above T_B , this is not the case along H_\parallel direction where a considerable fraction of spins are *blocked*. Below T_B at $T = 2$ K, $M - H$ curves show a wide hysteresis loop for field along H_\perp suggesting a highly oriented nature of the clusters. The Co nanoclusters possess an *easy* and *hard* axis of magnetization coupled with the magnetocrystalline anisotropy of the $\text{Ti}_{1-x}\text{Co}_x\text{O}_2$. In addition at $T=2$ K, surprisingly a crossover in the magnetization for two field directions in sample B and C is observed. The origin of this crossover is the anisotropic paramagnetism arising from the $2+$ ionic state of Cobalt in a $S = 3/2$ system. Role of dipole- interactions and inter-cluster exchange interactions have also been discussed.

TABLE I. T_B and parameters obtained by fitting $M - H$ data to the Langevin function are listed for H_{\perp} for samples A, B and C. T_B for H_{\parallel} is also mentioned

Sample	Fluence (ions/cm ²)	T_B (K) (H_{\perp})	T_B (K) (H_{\parallel})	Particle Size (nm)	σ	Average moment μ_M (μ_B)
A	5×10^{16}	30	8	2.50	0.3	1261.7
B	8×10^{16}	65	40	3.97	0.64	4562.8
C	1×10^{17}	150	70	4.43	1.25	6285.8

REFERENCES

- * shikha@iopb.res.in
- ¹ Alberto. P. Guimarães, Principles of Nanomagnetism, Springer-Verlag, Berlin, (2009).
 - ² T. Kaneyoshi, J. Phys. Cond. Mat. **3**, 4497, 1991.
 - ³ C. P. Bean and J. D. Livingston, Jour. Appl. Phys **30**, 120 (1959).
 - ⁴ K. Binder and A. P. Young, Rev. Mod. Phys. **58**, 801 (1986).
 - ⁵ F. C. Fonseca, G. F. Goya, R. F. Jardim, R. Muccillo, N. L. V. Carreño, E. Longo, and E. R. Leite, Phys. Rev. B **66**, 104406 (2002).
 - ⁶ F. Luis, J. M. Torres, L. M. Garcia, J. Bartolome, J. Stankiewicz, F. Petroff, F. Fettar, J.-L. Maurice, and A. Vaure's, Phys. Rev B, **65**, 094409 (2002).
 - ⁷ Adam J. Rondinone, Anna C. S. Samia and Z. John Zhang, J. Phys. Chem. B **103**, 6876 (1999).
 - ⁸ F. Wiekhorst, E. Shevchenko, H. Weller and J. Kötzler, Phys. Rev. B **67**, 224416 (2003).
 - ⁹ Y. Matsumoto, M. Murakami, T. Shono, T. Hasegawa, T. Fukumara, M. Kawasaki, P. Ahmet, T. Chikyow, S. Koshihara, and H. Koinuma, Science **291**, 854 (2001).
 - ¹⁰ K. Ueda, H. Tabata and T. Kawai, Appl. Phys. Lett. **79** 988 (2001).
 - ¹¹ T. Fukumura, Z. Jin, A. Ohtomo, H. Koinuma and M. Kawasaki, J. Appl. Phys. **75** 3366 (1999).
 - ¹² H. Ohno, A. Shen, F. Matsukura, A. Oiwa, A. Endo, S. Katsumoto and Y. Iye, Appl. Phys. Lett. **69** 363 (1996).
 - ¹³ K. W. Edmonds, K. Y. Wang, R. P. Champion, A. C. Neumann, N. R. S. Farley, B. L. Gallagher and C. T. Foxon, Appl. Phys. Lett. **81** 4991 (2002).
 - ¹⁴ D. H. Kim, J. S. Yang, K. W. Lee, S. D. Bu, T. W. Noh, S. J. Oh, Y. W. Kim, J. S. Chung, H. Tanaka, H. Y. Lee and T. Kawai, Appl. Phys. Lett. **81** 2421 (2002).
 - ¹⁵ J. Y Kim, J. H. Park, B. G. Park, H. J. Noh, S. J. Oh, J. S. Yang, D. H. Kim, S. D. Bu, T. W. Noha, H. J. Lin, H. H. Hsieh and C. T. Chen, Phys. Rev. Lett. **90** 017401 (2003).
 - ¹⁶ H. Toyosaki, T. Fukumura, Y. Yamada, K. Nakajima, T. Chikyow, T. Hasegawa, H. Koinuma and M. Kawasaki, Nature **3** 221 (2004).
 - ¹⁷ Y. Matsumoto, R. Takahashi, M. Murakami, T. Koida, X.-J. Fan, T. Hasegawa, T. Fukumura, M. Kawasaki, S.-Y. Koshihara and H. Koinuma, Jpn. J. Appl. Phys. **40** L1204 (2001).
 - ¹⁸ Jianping Xu, Shaobo Shi, Lan Li, Xiaosong Zhang, Yaxin Wang, Ximing Chen, Jianfeng Wang, Liya Lv, Fengming Zhang, and Wei Zhong, J. Appl. Phys **107**, 053910, (2010).

- ¹⁹ D. H. Kim, J. S. Yang, Y. S. Kim, T. W. Noh, S. D. Bu, S. J. Baik, Y. W. Kim, Y. D. Park, S. J. Pearton, J. Y. Kim, J. H. Park, H. J. Lin, C. T. Chen, and Y. J. Song, *Phys. Rev. B* **71**, 014440 (2005).
- ²⁰ W. T. Geng, Kwang S. Kim, *Phys. Rev. B* **68**, 125203 (2003).
- ²¹ Hongming Weng, Xiaoping Yang, Jinming Dong, H. Mizuseki, M. Kawasaki, and Y. Kawazoe, *Phys. Rev. B* **69**, 125219 (2004).
- ²² Y. Xin, J. Lu, P. A. Stampe, and R. J. Kennedy, *Appl. Phys. Lett.* **88**, 112512 (2006).
- ²³ M. E. Overberg, B. P. Gila, G. T. Thaler, C. R. Abernathy, S. J. Pearton, N. A. Theodoropoulou, K. T. McCarthy, S. B. Arnason, A. F. Hebard, S. N. G. Chu, R. G. Wilson, J. M. Zavada and Y. D. Park, *J. Vac. Sci. Technol. B* **20**, 969 (2002).
- ²⁴ Numan Akdogan, Alexei Nefedov, Hartmut Zabel, Kurt Westerholt, Hans-Werner Becker, Christoph Somsen, Şafak Gök, Asif Bashir, Rustam Khaibullin and Lenar Tagirov, *J. Phys. D, Appl. Phys.* **42**, 115005 (2009).
- ²⁵ R I Khaibullin, L R Tagirov, B Z Rameev, Sh Z Ibragimov, F Yildiz and B Aktaş, *J. Phys. Cond Mat* **16** L443 (2004).
- ²⁶ S. R. Shinde, S. B. Ogale, J. S. Higgins, H. Zheng, A. J. Millis, V. N. Kulkarni, R. Ramesh, R. L. Greene, and T. Venkatesan, *Phys. Rev. Lett.* **92**, 16601 (2004).
- ²⁷ J. F. Ziegler, M. D. Ziegler, J. P. Biersack, *Nucl. Inst. Meth. B* **268**, 1818 (2010).
- ²⁸ Shalik Ram Joshi, B. Padmanabhan, Anupama Chanda, V. K. Malik, N. C. Mishra, D. Kanjilal and Shikha Varma, *Applied Physics A*, **122**, 713, (2016)..
- ²⁹ E. Newnham, J. H. Fang and P. P. Santoro, *Acta Cryst.* **17**, 240 (1964).
- ³⁰ M. S. Park, S. K. Kwo, and B. J. Min, *Phys. Rev. B* **65**, 161201(R) (2002).
- ³¹ L. A. Errico, M. Renteria, and M. Weissmann, *Phys. Rev. B* **72**, 184425 (2005).
- ³² R. W. Chantrell, J. Popplewell and S. W. Charles, *IEEE Trans.on Magn. Vol. Mag-14*, 5, 975 (1978).
- ³³ Shengqiang Zhou, G. Talut, K. Potzger, A. Shalimov, J. Grenzer, W. Skorupa, M. Helm, J. Fassbender, E. Cizmar, S. A. Zvyagin, and J. Wosnitza, *J. Appl. Phys* **102**, 083907 (2008).
- ³⁴ Hongmei Luo, Donghai Wang, Jibao He and Yunfeng Lu, *J. Phys. Chem. B* **109**, 1919 (2005).
- ³⁵ M. Hanson, C. Johansson and S. Morup, *J. Phys. Cond. Mat* **5**, 725 (1993).
- ³⁶ G. Kresse and D. Joubert, *Phys. Rev. B* **59**, 1758 (1999).
- ³⁷ A. Ney, T. Kammermeier, K. Ollefs, S. Ye, V. Ney, T. C. Kaspar, S. A. Chambers, F. Wilhelm and A. Rogalev, *Phys. Rev. B* **81**, 054420 (2010).
- ³⁸ A. Ney, K. Ollefs, S. Ye, T. Kammermeier, V. Ney, T. C. Kaspar, S. A. Chambers, F. Wilhelm, and A. Rogalev, *Phys. Rev. Lett.* **100**, 157201, (2008).
- ³⁹ Weili Luo, Sidney R. Nagel, T. F. Rosenbaum and R. E. Rosensweig, *Phys. Rev. Lett.* **67**, 2721 (1991).
- ⁴⁰ D. Kechrakos, K.N. Trohidou, *Phys. Rev. B* **58**, 18, (1998).
- ⁴¹ D. Kechrakos, K.N. Trohidou, *J. Magn. Magn. Mat.* **262** 107 (2003).

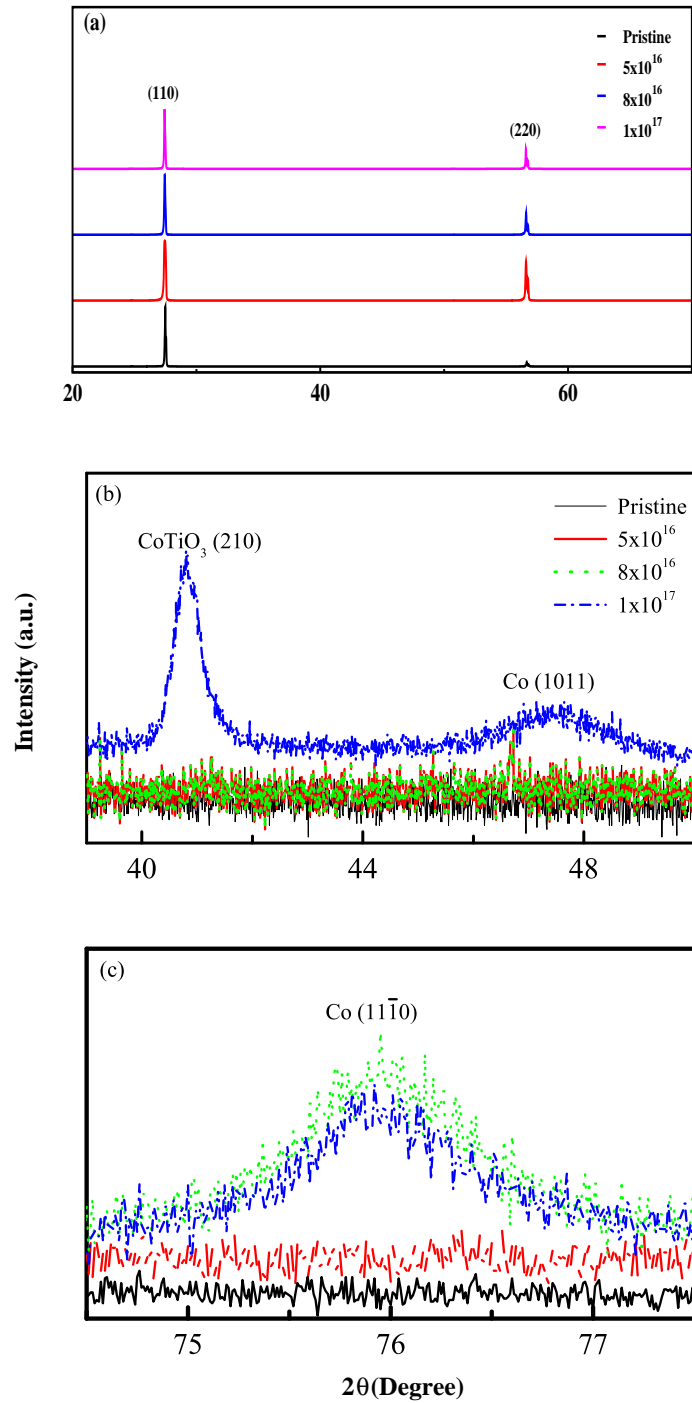


FIG. 1. (a) XRD in the normal $\theta - 2\theta$ geometry shows (a) [110] and [220] planes of TiO_2 (110) for the pristine and after Cobalt ion implantation (b) formation of Co clusters and secondary CoTiO_3 phase at the fluence of 1×10^{17} ions/cm² (c) Grazing incidence XRD showing Co clusters for 8×10^{16} and 1×10^{17} ions/cm².

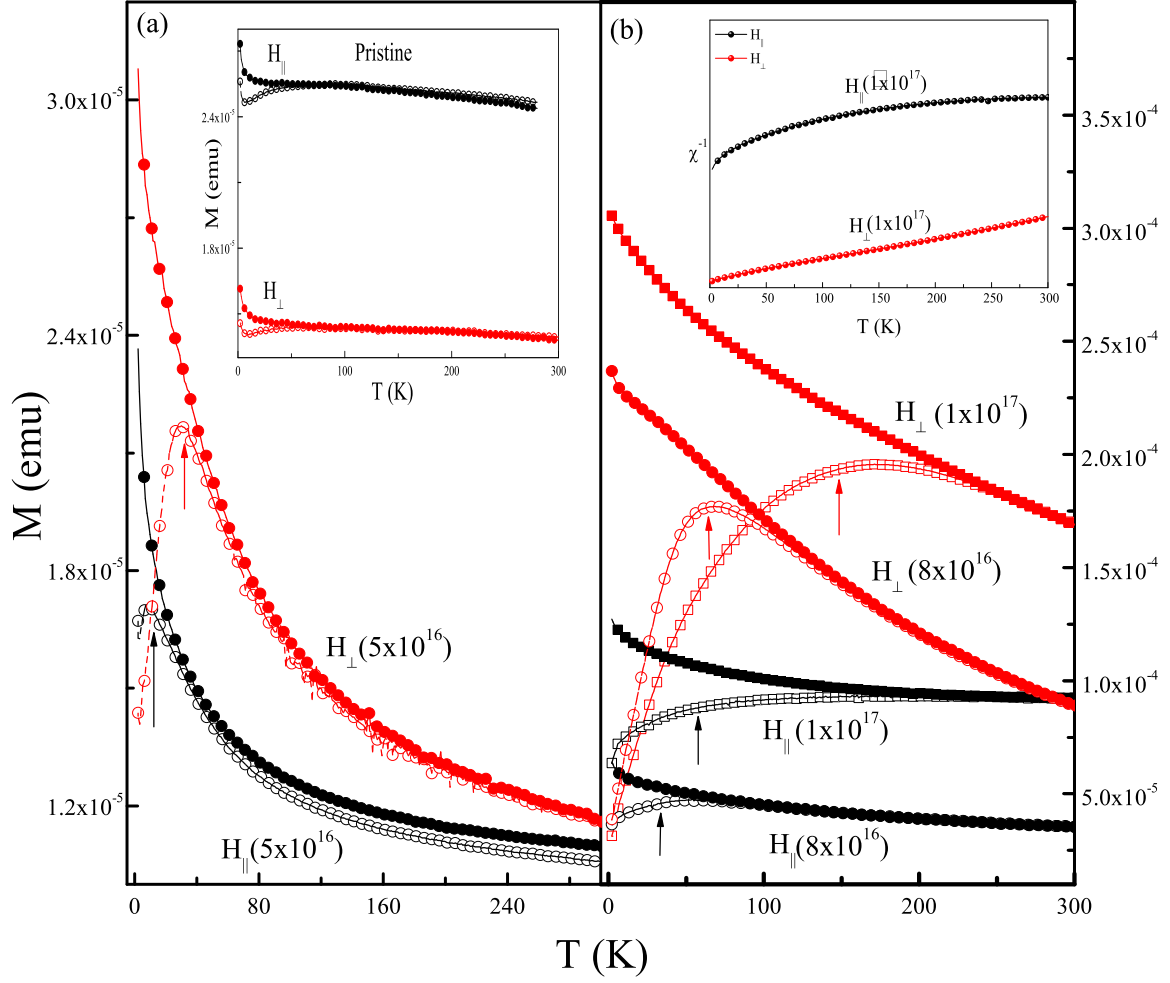


FIG. 2. ZFC (open symbols) and FC (closed symbols) graphs for cobalt implanted TiO_2 at 500 Oe for (a) sample A, inset shows for pristine. (b) samples B and C, inset shows χ^{-1} for sample C. The black and red symbols correspond to field parallel (H_{\parallel}) and perpendicular (H_{\perp}) to $\langle 001 \rangle$ directions of TiO_2 crystal. The arrows indicate the blocking temperatures.

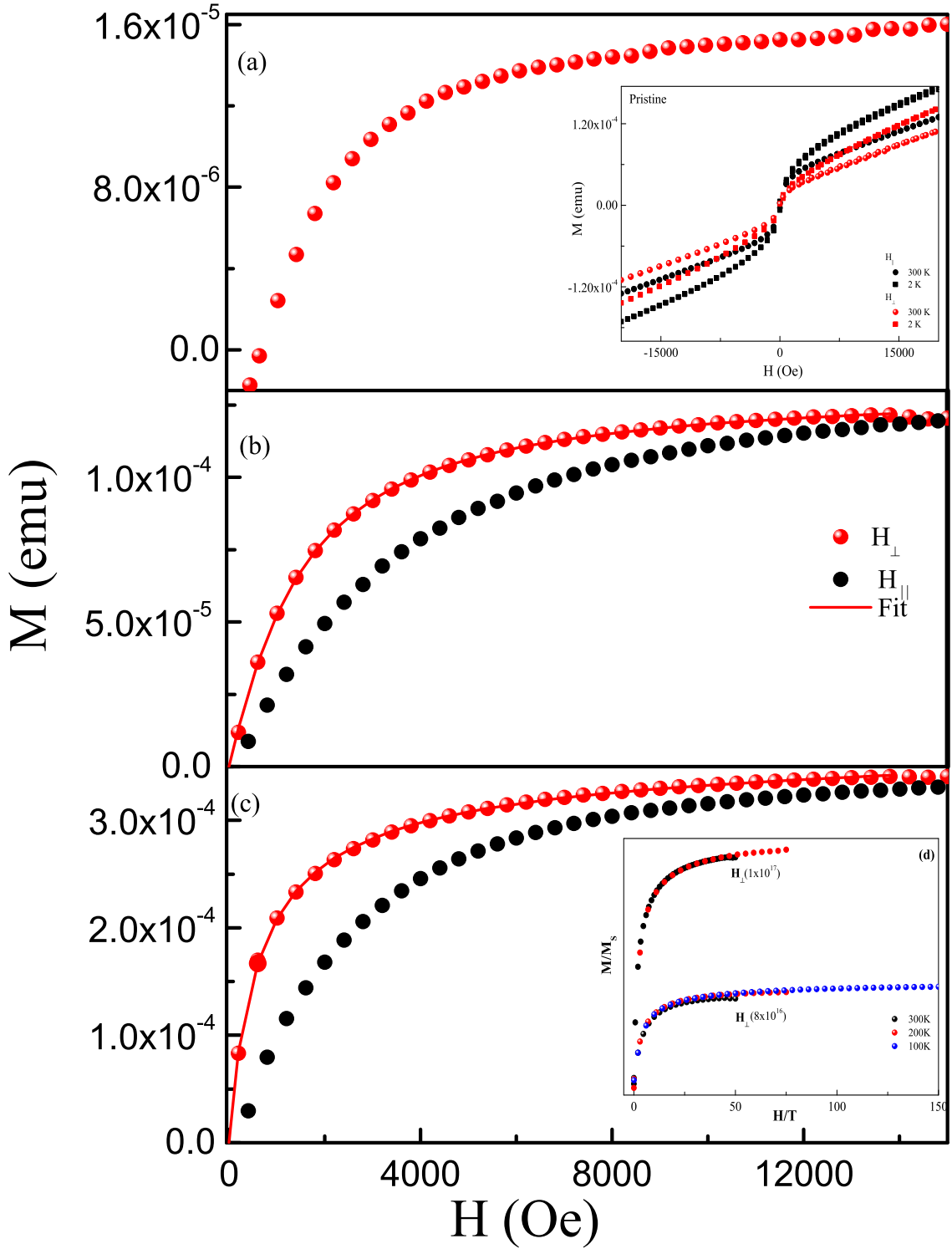


FIG. 3. Magnetization v/s Field graphs for Cobalt implanted TiO_2 for field along H_{\perp} (red symbols) and H_{\parallel} (black symbols). The solid curves correspond to fitting to Langevin function with lognormal distribution (eqn 2). In (a) data of sample A corresponds to $T = 100$ K. Inset shows the magnetization vs field of pristine sample obtained at $T = 300$ and 2 K, for both field directions. (b) Experimental and calculated (using eqn. 2) M - H plots at $T = 300$ K for sample B along both field directions. (c) Experimental and calculated (using eqn. 2) M - H plots at $T = 300$ K for sample C along both field directions. (d) Universal scaling behavior of samples B and C for field along H_{\perp} at various temperatures.

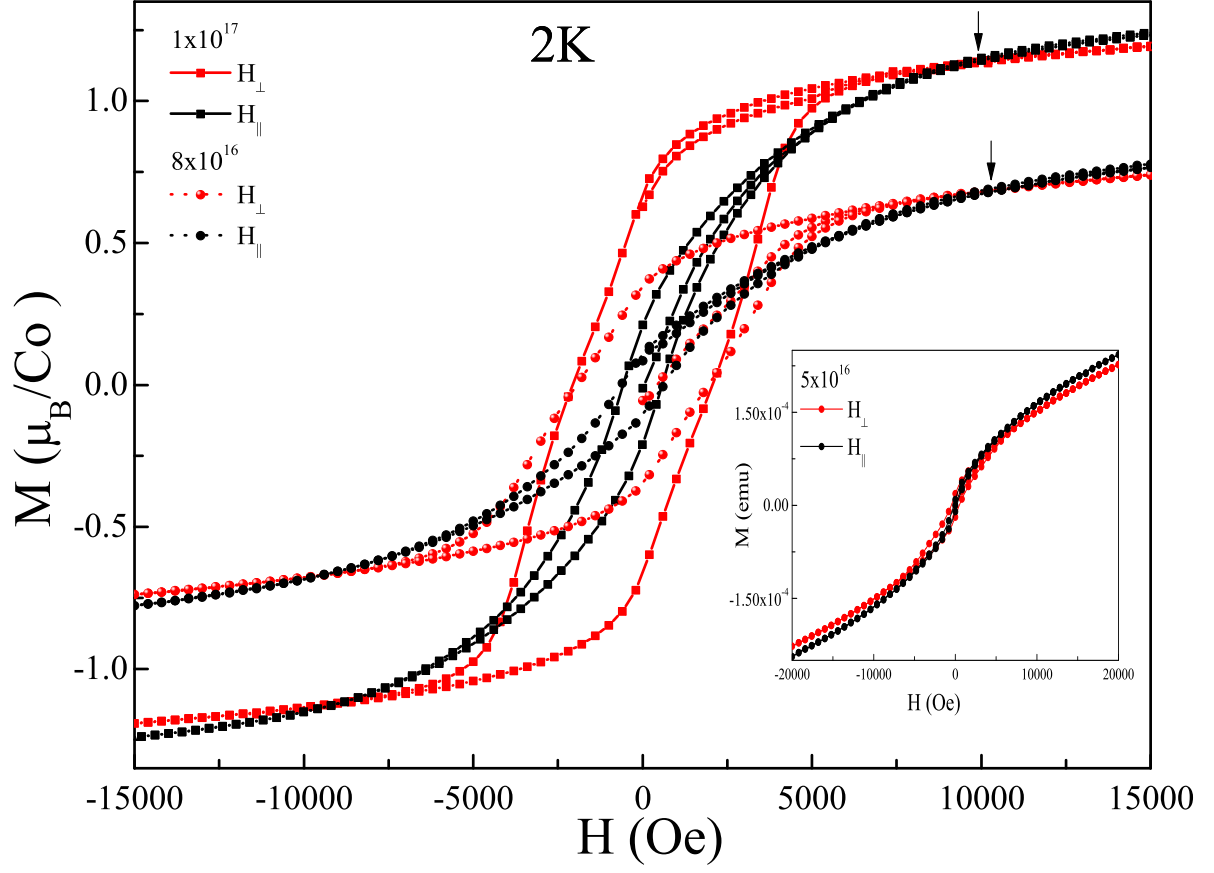


FIG. 4. M - H curves of samples B and C obtained at 2 K for fields along H_{\perp} (red symbols) and H_{\parallel} (black symbols). Arrows indicate cross-over. The inset shows M - H data for sample A at 2 K.

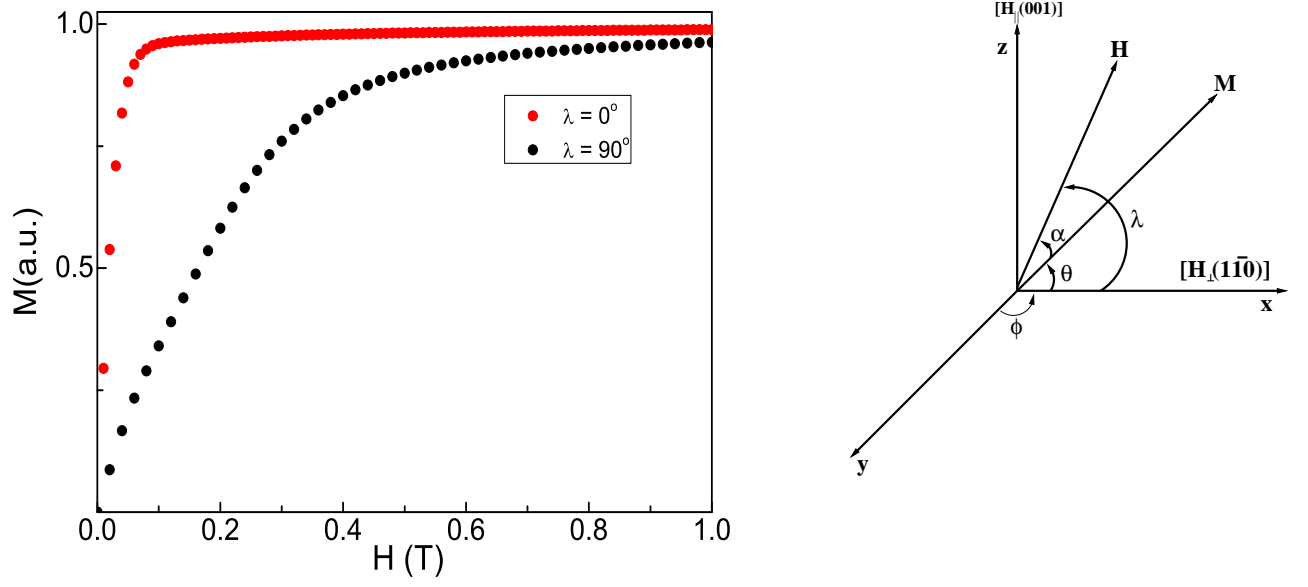


FIG. 5. M - H curves calculated for a single nanocluster for magnetic field applied along easy axis, $\lambda = 0^\circ$ (H_\perp) and hard axis, $\lambda = 90^\circ$ (H_\parallel) assuming complete saturation of the nano-particle with anisotropy constant $K_{mu} = 5 \times 10^6$ Joules/m³.

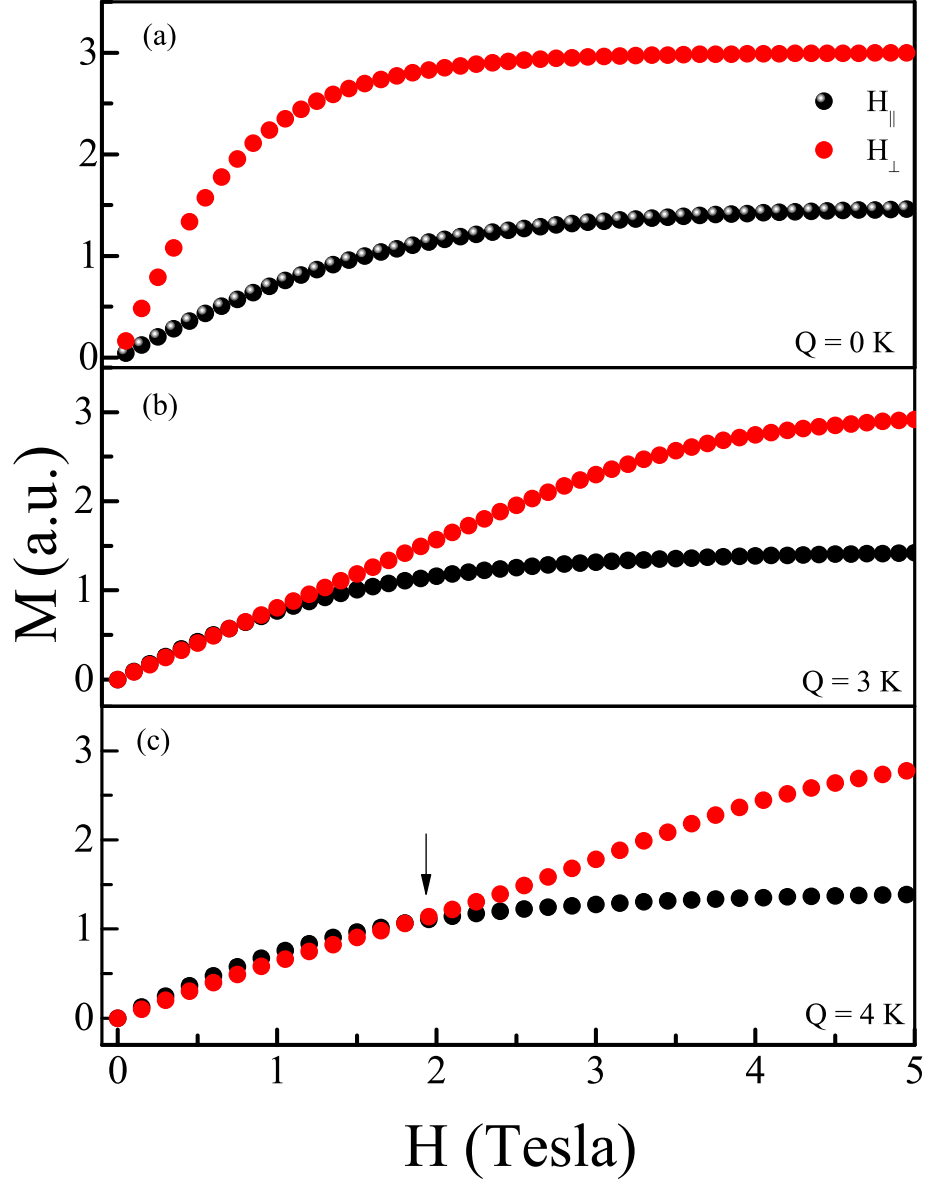


FIG. 6. Calculated M - H curves at $T = 2$ K for $H \parallel H_{\parallel}$ (black symbols) and $H \parallel H_{\perp}$ (red symbols) using effective spin Hamiltonian of eqn. (4) and different values of zero-field splitting Q . The anisotropy and the cross-over (marked by the arrow) between two field directions observed at $Q = 4$ K are similar to experimental results in Fig. 4

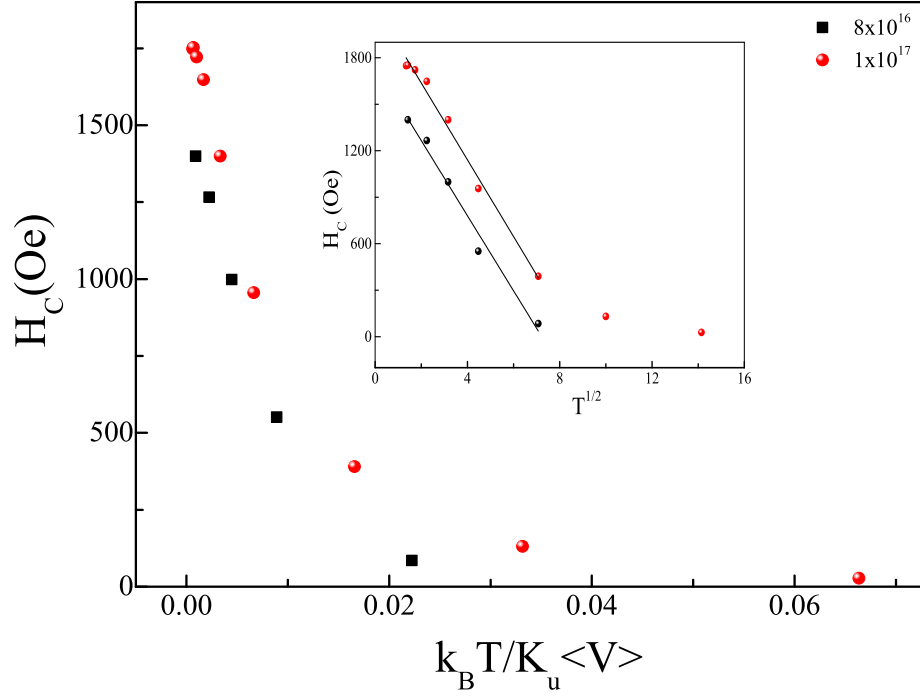


FIG. 7. H_C as a function of the reduced temperature $k_B T / K_u \langle V \rangle$, for samples B (square) and C (circle) for the field along the H_{\perp} direction. Inset displays H_C as a function of $T^{1/2}$ for samples B and C.